Journal of Atmospheric and Solar-Terrestrial Physics 104 (2013) 151–166

Contents lists available at ScienceDirect

Journal of Atmospheric and Solar-Terrestrial Physics

journal homepage: www.elsevier.com/locate/jastp

Temporal and spatial characteristics of the formation of strong noctilucent clouds

J. Kiliani *, G. Baumgarten, F.-J. Lübken, U. Berger, P. Hoffmann

Leibniz-Institute of Atmospheric Physics at Rostock University, Schlossstraße 6, 18225 Kühlungsborn, Germany

ARTICLE INFO

Article history:
Received 30 April 2012
Received in revised form
30 November 2012
Accepted 16 January 2013
Available online 4 February 2013

Keywords:
Noctilucent cloud
Summer mesosphere
Particle tracing
Visibility time
Growth characteristics

ABSTRACT

The 3-D Lagrangian model LIMA/ICE is used to track ice particles forming noctilucent clouds (NLC). Fifty strong NLC events at three different latitudes are analyzed. Visible particles are traced back to their nucleation sites as well as traced forward until sublimation. Particle nucleation occurs in bursts within areas of high supersaturation. We characterize NLC particle growth and vertical transport: Slow growth occurs below the mesopause up to $\approx$6 h before observation. It is followed by rapid growth within the high water vapor zone around 83 km during phases of upward winds. At the same time temperature perturbations in these cold phases of waves lead to a high supersaturation. Sublimation occurs quickly after maximum brightness, since sedimentation into subsaturated altitudes is accelerated by downward winds. The duration of particle visibility ($\beta > 10\%$ of observed backscatter) is only $\approx$5 h. The mean particle age of all NLC events at 69°N is around 36 h, but particle age varies by more than 24 h for the different events studied. Although the age of particles in strong NLC depends on latitude, the visibility period does not. The brightness of strong NLC depends mainly on background conditions during the last 3 h before observation. This implies that local measurements, e.g. by lidar, are representative for the morphology of strong NLC on scales of several hundred kilometers.

1. Introduction

1.1. Motivation

Noctilucent clouds (NLC) are the manifestation of ice particles in the polar summer mesosphere at altitudes of $\approx$83 km. In this region of the atmosphere, ice can only nucleate at temperatures below $\approx$150 K. This is often fulfilled around the mesopause from June to mid of August at northern polar latitudes, with a 6 month offset for SH. NLC may be seen by the naked eye at times when the middle atmosphere is still illuminated by the sun and the observer's position is in nautical twilight (e.g. Jesse, 1889). In the northern hemisphere this typically happens in the latitude band 50–65°N. A method for detecting NLC which does not depend on solar illumination is ground-based lidar measurements (e.g. Fiedler et al., 2009). NLC are also observable from satellites like the Aeronomy of Ice in the Mesosphere (AIM) satellite, which detects mesospheric ice by scattering of sunlight in the UV region (Cloud Imaging and Particle Size, CIPS) and by extinction of direct sunlight through the atmosphere at multiple wavelengths (Solar Occultation For Ice Experiment, SOFIE) (McClintock et al., 2009; Hervig et al., 2009; Russell et al., 2009).

The size of these particles ($\leq$100 nm) is much smaller than that of tropospheric ice clouds (Thomas and McKay, 1985). Since the scattering cross section of particles in this size regime at optical wavelengths is roughly proportional to r^5, mostly the larger particles ($r > 20$ nm) are visible to observers as well as optical instruments (i.e. cameras, lidars, spectrometers). Other instruments (i.e. radar, mass spectrometers, solar occultation) are capable of observing smaller ice particles that play a major role in generating polar mesospheric summer echoes (PMSE) which are often found together with NLC (e.g. Nussbaumer et al., 1996; Gumbel and Witt, 2001; Rapp and Lübken, 2004; Li et al., 2010; Kaifler et al., 2011).

Right now, there is no experimental method to directly trace the history of individual ice particles forming a noctilucent cloud. Only the ice clouds are temporarily observable as well as wind and temperature, within limits. A main reason for studying NLC is that they indicate extreme background conditions and are much easier to detect than those conditions themselves. Model studies suggest that NLC are formed at least several hundred kilometers away from the place of observation (e.g. Turco et al., 1982; von Zahn and Berger, 2003; Stevens et al., 2007; Merkel et al., 2009; Bardeen et al., 2010; Megner, 2011). Thus a detailed understanding of ice growth processes and origins is required to infer background conditions from NLC observations. Therefore we use modeling studies to examine origins, growth, and sublimation conditions of observed ice particles, as well as the factors determining their evolution.

* Corresponding author. Tel.: +49 38293 68124.
E-mail address: kiliani@iap-kborn.de (J. Kiliani).

1364-6826/$ - see front matter © 2013 Elsevier Ltd. All rights reserved.
http://dx.doi.org/10.1016/j.jastp.2013.01.005

1.2. Model description

In this study we use the Leibniz-Institute Middle Atmosphere (LIMA) model, a general circulation model with special emphasis on the mesosphere (Berger, 2008). LIMA adapts ECMWF reanalysis data in order to incorporate lower atmosphere effects. Thus it shows interannual variations like the solar cycle and trends, e.g. in temperature (Lübken et al., 2009). LIMA uses a triangular grid with a horizontal resolution of 110 km and a time step of 150 s.

There have been several model studies of NLC using the Community Aerosol and Radiation Model for Atmospheres (CARMA) on various circulation models. Examples are the Whole Atmosphere Community Climate Model (WACCM) (Bardeen et al., 2010; Merkel et al., 2009); the Navy Operational Global Atmospheric Prediction System (NOGAPS) (Stevens et al., 2010); and the Canadian Middle Atmosphere Model (CMAM) (Megner, 2011).

Our approach has some advantages compared to previous studies: While Bardeen et al. (2010) and Merkel et al. (2009) also use 3-D aerosol models that allow a continuous simulation over a time period of several months, similar to our approach, our Lagrangian model computes the particle trajectories in the same model run. This makes our model approach well suited for simultaneously investigating single particle evolution and ice development of the whole cloud. Since the cloud evolution strongly depends on the smaller scale variations in the atmosphere, our more realistic modeling of the background fields compared to COMMA/IAP is beneficial (Chandran et al., 2012; Berger and von Zahn, 2007).

In Fig. 1 we show the wind structure from LIMA compared with MF radar measurements at Andenes in Northern Norway (69°19′N, 16°18′E), similar to the data presented in Hoffmann et al. (2010). The radar measurements are 2 day mean winds after removing the 12 h and 24 h tides. These are compared with diurnal mean LIMA winds at the grid point nearest to Andenes. Since only ice clouds in the central NLC season are studied, we limit the wind comparison to the NLC season (June to August) and NLC altitudes (80–92 km). In this period, LIMA zonal winds are in general agreement with radar winds. We note that around 80 km, LIMA overestimates the mean zonal wind by ≈ 15 m/s, which is perhaps caused by deficiencies in the gravity wave parametrization. This deviation is present at most altitudes, but is less pronounced near the mesopause (≈ 90 km). Mean meridional winds agree very well at 83 km, while further up the radar southward wind is stronger by up to ≈ 6 m/s. Radar measurements also show a higher variability compared to LIMA. We discuss the implications of these differences later in Section 3.1.2. Generally, we expect westward transport in LIMA being somewhat too strong, southward transport being slightly too weak. The lower variability in LIMA horizontal winds suggests that vertical wind variations are also underestimated to some extent.

To model noctilucent cloud formation, we employ the three-dimensional Lagrangian ice transport model LIMA/ICE (Lübken et al., 2009). NLC formation is simulated by advecting 40 million condensation nuclei ("dust particles") in wind and temperature fields supplied by LIMA at a time step of 180 seconds. The dust particles range in radius from 1.2 to 3.7 nm, forming the larger

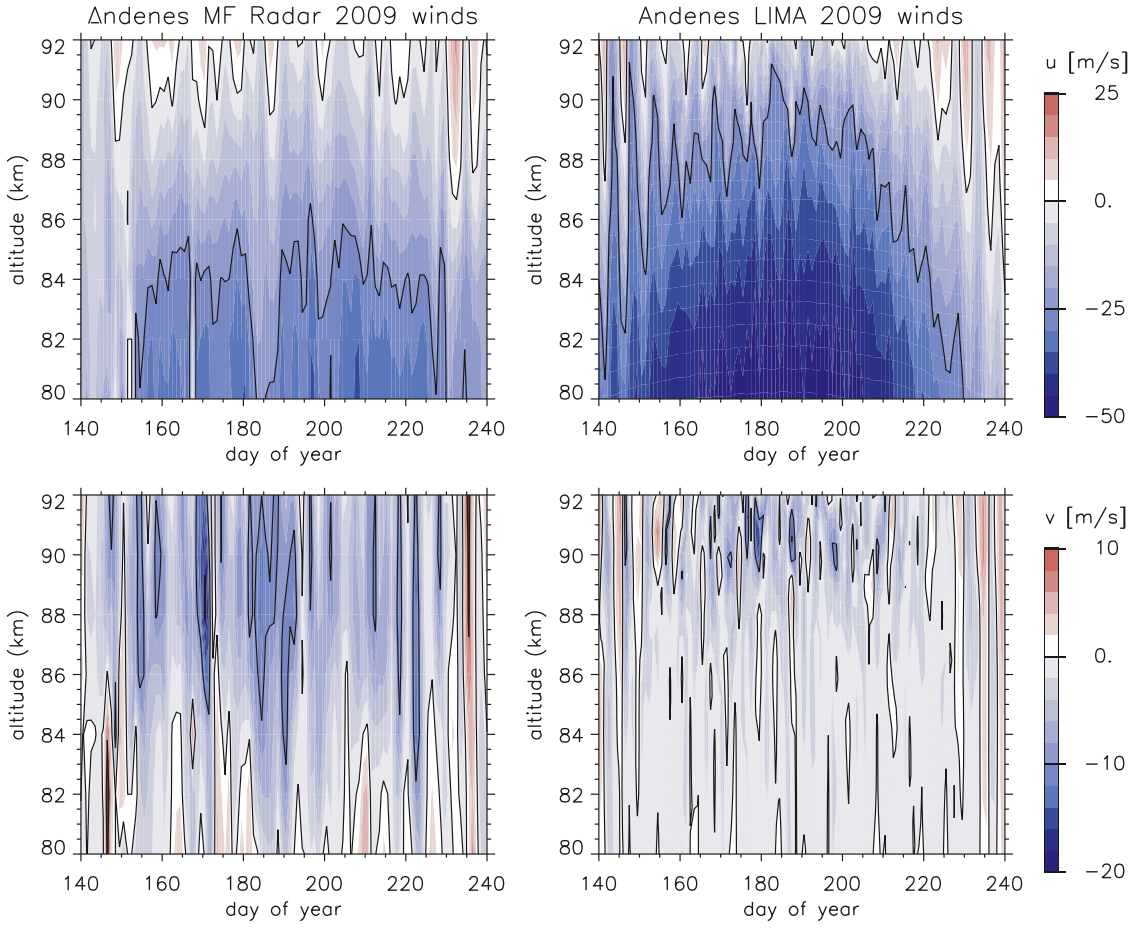

Fig. 1. Summer 2009 wind profiles at Andenes (69°N), zonal (upper) and meridional (lower). Left side: Residual winds of a 2-day fit removing diurnal and semidiurnal tides from MF radar measurements. Right side: diurnal mean LIMA winds.

dust sizes of the log distribution from Hunten et al. (1980). Furthermore, condensation nuclei are continuously relocated in the model domain, for more details see von Zahn and Berger (2003). LIMA/ICE includes a chemistry transport model for water vapor, including H_2O photolysis by solar Lyman$_\alpha$ radiation. LIMA/ICE is limited to polar and middle latitudes of the Northern (May through August) and Southern (November to February) Hemisphere, since NLC only appear in the polar summer mesosphere. The chemistry transport module uses a grid size of 1° latitude, 3° longitude and 100 m vertical resolution, ranging from 78 to 94 km. In LIMA/ICE, NLC distribution is calculated using the backscatter coefficient at a wavelength of 532 nm. This facilitates comparison with NLC detection by lidars. NLC formation as modeled by LIMA is in general agreement with observations, concerning height, latitudinal extent and long-term variations (Lübken et al., 2008; Lübken and Berger, 2011; Lübken et al., 2009). In this study we focus on strong NLC, since they are much more likely at their peak brightness (in the stationary phase) and not in the growth or decline phase. This also facilitates a comparison with measurements, because strong NLC are easier to detect by optical methods (lidar, satellite).

We validate the size of ice particles as calculated by LIMA by comparing with lidar three-color measurements of strong NLC observed between 1998 and 2009 at ALOMAR (Baumgarten et al., 2010). We compare color ratios directly by calculating these from LIMA, using optical modeling. We do not compare LIMA particles with particle size values derived from these measurements, since the latter depend on assumptions about the size distribution. LIMA/ICE simulates spherical particles only, which for most purposes is a reasonable simplification. However, we need to take non-spherical particles into account when calculating the optical signal (“color ratios”) (Baumgarten and Thomas, 2006; Rapp et al., 2007). In Fig. 2 we show the distribution of color ratios of a large number (125,000) of sample volumes within LIMA ice clouds at 69°N and corresponding lidar results. For the LIMA color ratios, we assume spheroid particles with a shape distribution of spherical, oblate, and prolate particles up to an aspect ratio of 10 which is also used by the ALOMAR lidar retrieval method (Baumgarten et al., 2007). This ensemble gives a mean axis ratio distribution of 3.9. We only use the color ratios of those sample volumes where the backscatter coefficient at 532 nm exceeds 10% of the maximum value. This is analogous to the procedure when evaluating lidar data, since below some threshold the measurement uncertainty becomes too large. To make these model results comparable to measurements, we also have to take into account measurement uncertainties. We added a normally distributed random number to each model color ratio, using the variabilities of the lidar distribution. We found the best agreement when the variability of this random number was reduced by 30% to account for the variability already included in the LIMA color ratio distribution. This distribution is shown in the middle panel of Fig. 2. It compares well to the measured distribution (lower panel), which implies that LIMA NLC particles are of similar size compared to measurements. When comparing the mode of the measured and modeled distribution we find a nice agreement in the color ratio of 355–532 nm which is 2.92 and 2.91 in the observations and model, respectively. The color ratio 1064–532 nm is 0.94 and 0.89 respectively. The slight deviations could be caused by the fact that the lidar observations include a larger set of data (1998–2009) with a natural variability larger than the variability of the 50 LIMA NLC used in the current analysis. We have also compared the model results to the lidar using an axis ratio distribution similar to that observed by SOFIE measurements (Hervig and Gordley, 2010; Hervig et al., 2009) (mean about 2 and variance of about 0.6). We found the mode of the color ratio distribution at 2.95 and 0.81 for the 355/532 and 1064/532 color ratio, respectively. While the 355/532 color ratio is still pretty close to the observation, the agreement in the 1064/532 gets worse. So we find that the lidar data is better reproduced when using a axis ratio distribution holding more non-spherical particles. We conclude that LIMA NLC particle size agrees well with lidar data. It would be advantageous to fully incorporate particle shape in the model, which would give a larger variability in the modeled particle sizes due to different growth rates, similar to an increased variability in the background conditions.

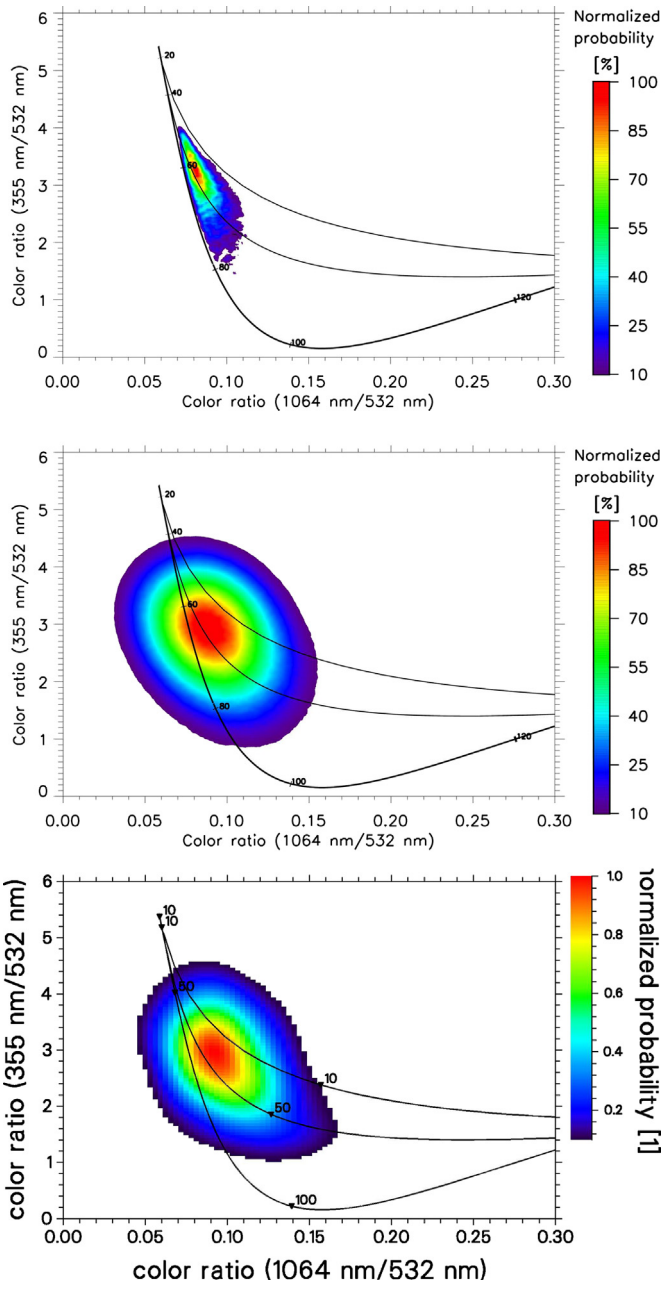

Fig. 2. Modeled color ratio distribution within strong LIMA ice clouds at 69°N using spheroidal particles and measured color ratios from ALOMAR. Solid lines shows color ratios of monodisperse distributions of spherical particles (radius in nm), as well as color ratios of lognormal distributions of spherical particles with $\sigma = 1.4$ (middle line) and $\sigma = 2$ (upper line). Upper panel: Simulation of model color ratios as measured by a perfect lidar, using LIMA results. Middle panel: Model color ratios assuming an error derived from lidar measurements. Lower panel: Multi-year lidar measurements of color ratios of strong NLC at ALOMAR.

2. Analytical techniques

We study the development of ice clouds by (a) selecting time slots where strong NLC occur at the observation site, (b) selecting a number of 40,000 ice particles in each time slot which cause nearly the entire backscatter signal at observation ($\approx 99\%$), and (c) tracing those particles for the duration of their individual lifetime.

2.1. NLC event selection

We choose a number of ice events in LIMA representing strong NLC in the northern hemisphere. From this selection, we trace the largest ice particles from nucleation to sublimation, chosen so that they represent the visible part of these ice clouds. We decided on a number of 50 cases within July 2009, since strong NLC are most common in mid season.

For comparability with measurements, we restrict the location of the NLC events to three areas at different latitudes. The first two were chosen around sites with Lidar and Radar measurements, namely Ny-Ålesund on Spitsbergen (78°N, 11°E) and ALOMAR in Northern Norway (69°N, 16°E) (Höffner and Lübken, 2007; Fiedler et al., 2009). In these two cases, we chose sample areas limited by longitude and latitude and $\approx 300{,}000\ \mathrm{km}^2$ large. Latitudinal size is 5° in both cases, longitudinal size is 24° for Spitsbergen and 15° for ALOMAR, centered around the locations. The third area consists of sectors, limited by the 60°N latitude circle in the North and 15° wide in longitude. The longitude range is chosen individually around the brightest ice cloud south of 60°N, these rarely extend beyond 55°N. This is necessary because strong NLC events this far south are so rare that NLC at a fixed location would not have yielded robust statistics over one season. Thus the third area varies in location and is larger than the other two. We chose two fixed positions instead of latitudinal bands because there is extensive measurement data available there. LIMA shows a longitudinal dependence of local time temperature variations, but this dependence is not very well covered by measurements. Since the causes of the tidal signal are not well known, we opted for the approach used here.

For the ALOMAR case, we show the hourly NLC brightness ($\beta_{\max}, \lambda = 532$ nm) in July 2009 in Fig. 3. We choose 50 events at a time interval of 1 h when the backscatter signal is highest, as marked in Fig. 3. This gives us a selection of 14 continuous NLC with a total duration of 50 h and a brightness threshold of $\beta_{\max} > 21.5 \times 10^{-10}\ \mathrm{m}^{-1}\ \mathrm{sr}^{-1}$. The NLC are not uniform in duration, but range from 1 h to 6 h above the threshold. This implies that NLC with longer duration have a greater weighting in the statistics we derive. This procedure was applied following the analysis methods used for lidar or radar observations (Fiedler et al., 2009). It should be noted that at ALOMAR, the NLC local time variation in the model agrees nicely with lidar measurements: In Fig. 3, occurrence rates peak at 2–6 UT, corresponding to 3–7 local time. Fig. 4 in Fiedler et al. (2011) also shows that strong NLC typically occur in the morning hours, and only a few occur in the afternoon. A more detailed comparison is shown in Lübken et al. (2013) for $\beta_{\max} > 4 \times 10^{-10}\ \mathrm{m}^{-1}\ \mathrm{sr}^{-1}$. For these brighter NLC and a longer dataset than used here, the agreement in occurrence rates is satisfactory.

For 78°N, the selection process is analogous to 69°N, but because of generally stronger NLC here, the $\beta_{\max}$-threshold is $47 \times 10^{-10}\ \mathrm{m}^{-1}\ \mathrm{sr}^{-1}$ in this case. For latitudes south of 60°N, there are generally weaker NLC, resulting in a threshold brightness of only $1.2 \times 10^{-10}\ \mathrm{m}^{-1}\ \mathrm{sr}^{-1}$. In total, we selected 150 NLC events, 50 for each latitude. Most of these belong to NLC lasting for more than 1 h, resulting in ≈ 15 separate NLC per latitude band.

2.2. Ice particle selection

For computational reasons, we decided to trace 40,000 of the largest LIMA ice particles for each NLC event and not all of them. This number was chosen such that the backscatter signal from those particles contributes a high percentage of the total backscattering within the selection area, typically 99%. For each ice event, we calculated the ratio of the backscattering generated by those 40,000 large ice particles to the whole backscatter signal in the selection area: For the two selection boxes at ALOMAR and Spitsbergen, this ratio is generally greater than 90%, in most cases more than 99%. Only for the larger selection area south of 60°N, it

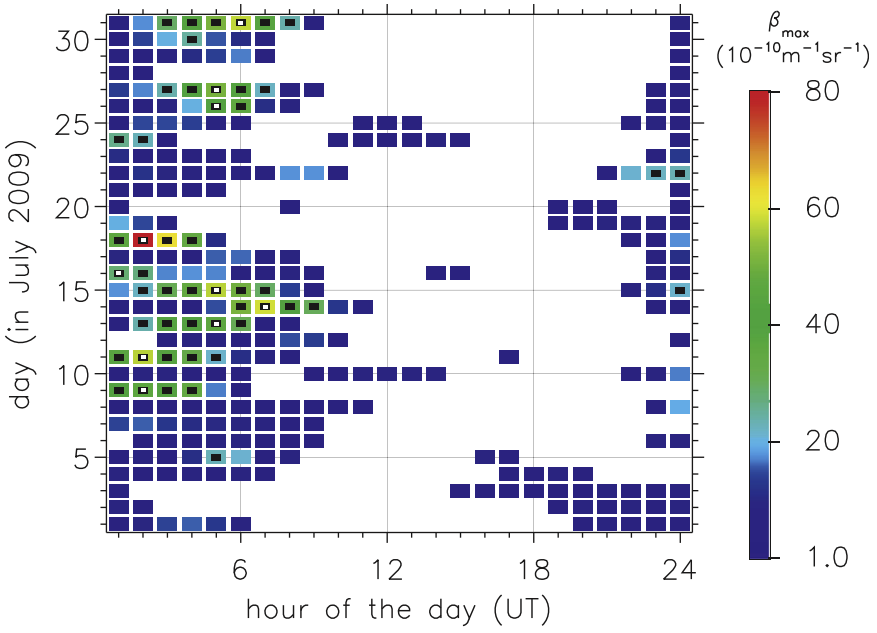

Fig. 3. LIMA peak backscatter coefficient around ALOMAR for July 2009. The threshold is $\beta_{max} > 1 \times 10^{-10}\ \mathrm{m}^{-1}\ \mathrm{sr}^{-1}$. Fifty time indices where $\beta_{max} > 21.5 \times 10^{-10}\ \mathrm{m}^{-1}\ \mathrm{sr}^{-1}$ and which were subsequently marked as an NLC event used for particle tracing are marked in black. These 50 time indices of NLC events belong to 14 different NLC (different meaning there is at least 1 h without NLC in between). The times of peak brightness of the 10 strongest NLC are marked in white.

is slightly lower. The mean value of the ratio is 99.5% for ALOMAR, 98.7% for Spitsbergen and 96.3% south of 60°N. The selected particles are distributed in an altitude range of about 81–88 km, most of them are found at about 84 km. When weighting the particles with their optical signal (Section 2.3) we find that the distribution is narrow, about ± 1 km around the altitude of maximum brightness. The traced particles are thus highly representative of the history of the visible part of the NLC in question.

2.3. Trajectories

LIMA/ICE normally simulates NLC formation in a whole hemisphere by modeling nucleation, growth, transport, and sublimation of a sample of 40 million condensation nuclei. For our analysis we consider only those 40,000 particles described above at a temporal resolution of 3 min. From these trajectories we consider only those parts when the condensation nuclei are coated with ice, i.e. pure dust particles are not included in our statistics.

The result of our analysis is the time series of mean values and distribution width of particle radius, position, and background conditions. We note that the Lagrangian analysis describes the ice cloud in a moving frame of reference, not a stationary one like most types of measurements. For instance, particle visibility times calculated in this manner are not necessarily comparable with the time span that a NLC is present at a fixed location. The sample size of the distribution grows whenever ice particles nucleate. The sample is largest at the time of particle selection (t_0), from this point on it diminishes when the particles sublimate. A consequence is that at the beginning of the time series, very few particles contribute to the average. For the larger part of our analysis, we combine the history of 50 NLC events in a superimposed epoch analysis with reference time t_0. In the following we call the time t_0 also "NLC observation", e.g. times before observation have $t < t_0$.

We also trace the development of particles in both time directions until certain conditions are reached (e.g. beginning of nucleation). At these points in time, we analyze parameters like position and ambient temperature. This gives us histograms, usually two-dimensional, of the ice particles' state at particular times.

For most of our statistical data, we weight particles by their backscatter signal at 532 nm at observation (t_0). We call this 'signal-weighted mean' in the following and denote it as "method I". In this way, the derived statistics are representative of the ice particles contributing to the optical signal seen by lidar. In contrast, unweighted mean values of the 40,000 particles (method II) describe the state of the large number of smaller ice particles. Results from method II are sensitive to the number of traced particles, so they are used for qualitative analysis and comparison purposes only.

3. Results and discussion

3.1. NLC development at 69°N

We first show the development history of a single NLC which arrives around ALOMAR (69°N, 16°E) on July 14, 7 UT. After this, we discuss more general results using the superimposed epoch analysis.

3.1.1. Development of a single NLC at 69°N

In Fig. 4 we show the temporal evolution of the position and shape of the strong NLC arriving on July 14, 7 UT around ALOMAR. We have also selected 10 single particle trajectories by randomly

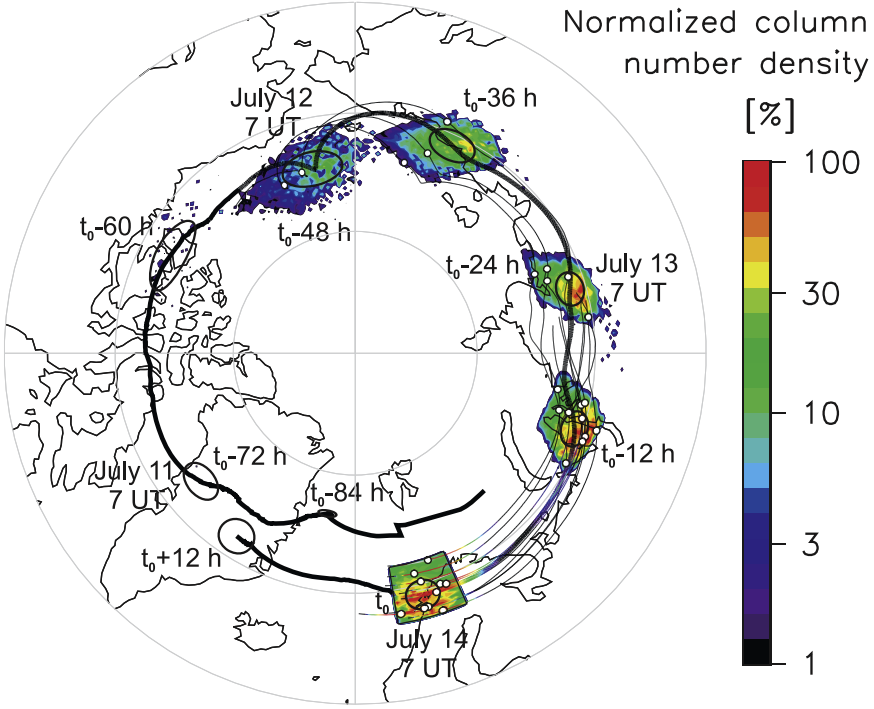

Fig. 4. Trajectory of an NLC observed at ALOMAR (69°N, 16°E) on July 14, 7 UT ($=t_0$). The color contours show snapshots at 12 h intervals of particle column number density, weighted by backscatter signal at t_0 and normalized to maximum bin occupancy. At t_0, the contours thus indicate NLC brightness distribution within the selection volume. The ellipses show mean position and zonal/meridional distribution width at the 12 h intervals. The thick line is the mean path of all particles forming the NLC, starting at the time of the earliest nucleations and ending when most particles have sublimated. Line color indicates cloud backscatter signal, as a percentage of observed BSC, on the same color scale as number density. Black lines mean particles are present, but not visible at this time. The thin lines are 10 individual particle trajectories, with the dots marking the positions at the snapshot intervals. (For interpretation of the references to color in this figure caption, the reader is referred to the web version of this article.)

picking particles out of the 40,000. The transport is mainly directed westward with a slight southward drift. We note that the backtraced NLC has a high spatial coherence more than a day before its observation. This is also visible from the single trajectories, which are nearly parallel to each other. The backtraced NLC has a vertical extent of about 4 km (shown later in Fig. 5). The reason for the horizontal dispersion (the smearing at the edge of the backtraced NLC) is that particles at different altitudes are exposed to different horizontal winds, while the NLC's changing shape is caused by horizontally inhomogeneous winds.

The individual particles nucleate at very different times, visible both from the single particles' starting points and the changing column number densities. As can be seen from the jump in number density on July 12, 7 UT, most particles nucleate on July 12 or later, so they are less than 60 h old when they are observed. While we show the mean trajectory before that point, very few particles contribute to the mean at that stage. Particle age will be discussed in more detail in Section 3.2. We note also that the mean transport path shows an oscillation in the meridional, caused by transport through atmospheric waves.

In Fig. 5, we show particle properties and ambient parameters most influential for determining growth or sublimation of icy particles. Here p_{H_2O} is the ambient vapor pressure, while the equilibrium vapor pressure p^*_{sat} includes the Kelvin effect and particle temperature and thus depends on particle properties and ambient parameters (temperature, pressure, etc.) (Pruppacher et al., 1978; Espy and Jutt, 2002).

First, we notice that ice particles grow slowly and steadily in the beginning ($dr/dt = 0.3$ nm/h typically), with only minor variations of background conditions. This phase in particle growth takes place more than 24 h before observation, at altitudes of $\approx$88 km and ambient temperatures around 130 K. During this time, much of the particles' vertical motion is caused by turbulence, which leads to a large variance of ice particles within the NLC, in altitude and ambient background conditions (Berger and von Zahn, 2002). This is evident in the single particle trajectories, and even in the mean trajectory before $\approx t_0-72$ h. After about t_0-24 h, particle growth is increasing to $dr/dt > 0.5$ nm/h and is more and more influenced by variations in background conditions, resulting in periods of partial sublimation. Finally, the main growth phase from 20 to 60 nm occurs within $\approx$4 h to observation, growth rate reaches to 15 nm/h then. During the main growth phase, sedimentation velocity increases with increasing particle mass, and upward and downward turbulent motion decreases, as the particles are found below the area of peak turbulence (detailed discussion in Section 3.1.2). Sublimation after the NLC observation is even faster ($dr/dt = -60$ nm/h), so it takes only $\approx$2 h until $\beta < 1\%$ of the value at observation. Only during a few hours from t_0-4 h to t_0+2 h is the backscatter signal larger than 1% of the observed value. The time interval between exceeding and falling below 50% of signal maximum is only slightly over 2 h, with growth and sublimation times of $\approx$70 min and 60 min, respectively. This growth characteristic is typical for large particles.

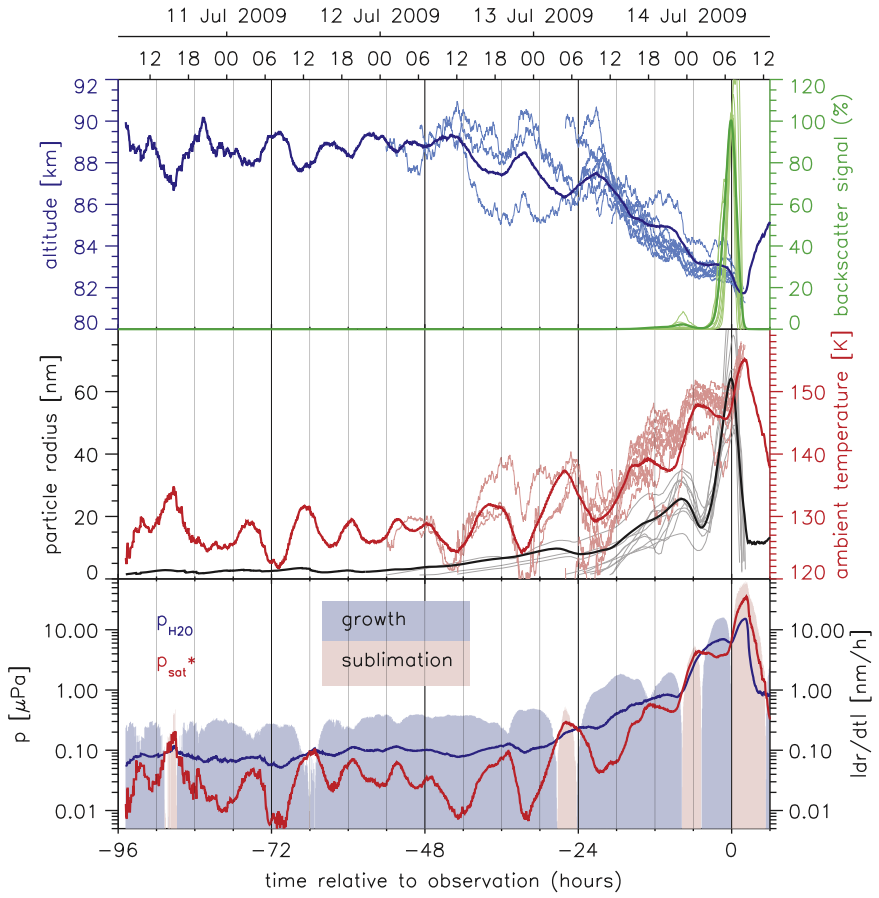

Fig. 5. Temporal evolution of ice particles forming the same NLC as in Fig. 4 (July 14, 7 UT). Upper panel: Mean altitude and total NLC backscatter signal, middle panel: mean ambient temperature and radius, lower panel: ambient H_2O partial pressure and equilibrium vapor pressure. All mean values are weighted with the particles' backscatter signal at the time of observation. The thin lines (upper and middle panel) represent the same for 10 large particles as in Fig. 4. The shading in the lower panel shows mean radius change rate (blue while growing, red while sublimating). (For interpretation of the references to color in this figure caption, the reader is referred to the web version of this article.)

Going into more detail, we investigate the variations in the background conditions and their effects on particle growth. Temperature and saturation pressure show an oscillation with a period of ≈ 10 h and peak-to-peak amplitudes of up to 10 K, causing equilibrium saturation pressure variations reaching a factor of 20 (Fig. 5). These oscillations are caused by particle transport through a combination of tides and other mechanisms (e.g. gravity waves). The exact composition is still under investigation, at the moment we assume that tides constitute a large part of the variability and that gravity waves are not resolved completely. Particle growth is closely influenced by these oscillations: Nucleation of new particles typically occurs whenever ambient temperature is decreasing (see Section 3.2.1), and particle growth is fastest while temperature is near minimum. This is most apparent when considering single particle trajectories. NLC mean particle radius may actually decrease in periods of supersaturation (e.g. around t_0-58 h) due to a lot of new ice particles forming, which are not included in the mean before that time. This also means that the mean growth rate in the lower panel of Fig. 5 is identical to the slope of mean radius only while no new particles are forming.

The effects of the oscillations on particle growth increase with time, when ice particles enter lower altitudes. The reason for this can be seen by the following, simplified relationship for the growth rate of ice particles (Turco et al., 1982):

$$\frac{\mathrm{d}r}{\mathrm{d}t} \propto p^*_{\mathrm{sat}}(S^*-1) = (p_{\mathrm{H_2O}} - p^*_{\mathrm{sat}}) =: \Delta p^* \quad (1)$$

where $S^* = p_{\mathrm{H_2O}}/p^*_{\mathrm{sat}}$ is the particle saturation ratio. The water vapor equilibrium pressure $p^*_{\mathrm{sat}} \propto e^{-6077.4\ \mathrm{K}/T_p}$ is also dependent on particle radius (Kelvin effect) and the particle temperature T_p. T_p is higher than ambient temperature (up to ≈ 3 K) because of radiative (infrared) particle heating. From Eq. (1) we see that the actual difference of the pressures Δp^* determines growth and not the ratio S^*.

Until 30 h before NLC observation, $p_{\mathrm{H_2O}}$ varies between 0.08 and 0.12 μPa, p^*_{sat} between 0.01 and 0.1 μPa. The typical water vapor pressure surplus of $\Delta p^* = 0.06$ μPa leads to a growth rate of only 0.3 nm/h, even though S^* may surpass 10 (at t_0-43 h, t_0-32 h). In contrast, during the peak of the main growth phase 2 h before observation, we have $p_{\mathrm{H_2O}} = 6.7$ μPa and $p^*_{\mathrm{sat}} = 3.6$ μPa, thus $\Delta p^* = 3.1$ μPa and $\mathrm{d}r/\mathrm{d}t = 15$ nm/h, while $S^* \approx 2$. Around observation time, saturation pressure grows so quickly that it is no longer compensated by the increase in water vapor, and the ice particles start to sublimate: 2 h after observation, we have $p_{\mathrm{H_2O}} = 15$ μPa and $p^*_{\mathrm{sat}} = 31$ μPa, giving $\Delta p^* = -16$ μPa and a sublimation rate of $\mathrm{d}r/\mathrm{d}t = -56$ nm/h.

We conclude that the main particle growth occurs when the ambient water vapor surplus to saturation pressure reaches its maximum. Rapid growth followed by sedimentation and sublimation also causes a vertical redistribution of mesospheric water vapor. This enhances the water vapor concentration at NLC altitudes and supports the growth of subsequent ice particles provided that the air is super saturated (Lübken et al., 2009).

3.1.2. Ensemble mean development at 69°N

We now broaden our study to include the backtrajectories of all 50 NLC events. First, we show the mean path of this 50 event ensemble in Fig. 6, in addition to the mean trajectories of 10 individual NLC. The general direction of transport is very close to the example in Fig. 4. The spatial extent of this superimposed ice cloud is larger than that of the single NLC because the wind fields transporting these different ice clouds vary to some extent, as can be estimated by looking at the wind variation in Fig. 1. This is apparent when comparing the superimposed cloud at t_0-36 h in Fig. 6 with the cloud on July 12, 19 UT in Fig. 4 for instance. The wind variability can also be seen by the $\Delta t = 12$ h horizontal variability ellipses or by the single cloud trajectories and their $\Delta t = 12$ h location markers. Dispersion is taking place mainly in

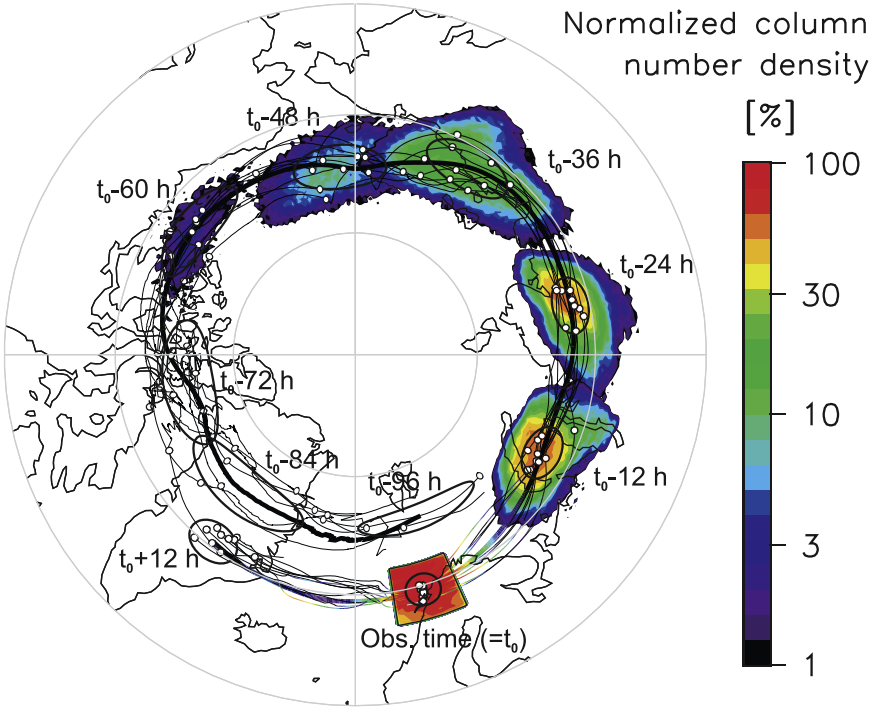

Fig. 6. Analoguous to Fig. 4, but showing mean path and snapshot cloud positions of all 50 NLC events observed around ALOMAR, with a superimposed epoch analysis. The contours show snapshots at 12 h intervals. The thick line shows signal-weighted mean position of all particles from 50 ice clouds, while the thin lines are mean paths of 10 out of 50 individual NLC. Line coloring indicates ensemble or individual NLC brightness, as in Fig. 4. The ellipses show ensemble mean position, plus zonal and meridional distribution widths of the ensemble at the 12 h snapshots, while the dots are individual NLC mean positions at 12 h intervals. (For interpretation of the references to color in this figure caption, the reader is referred to the web version of this article.)

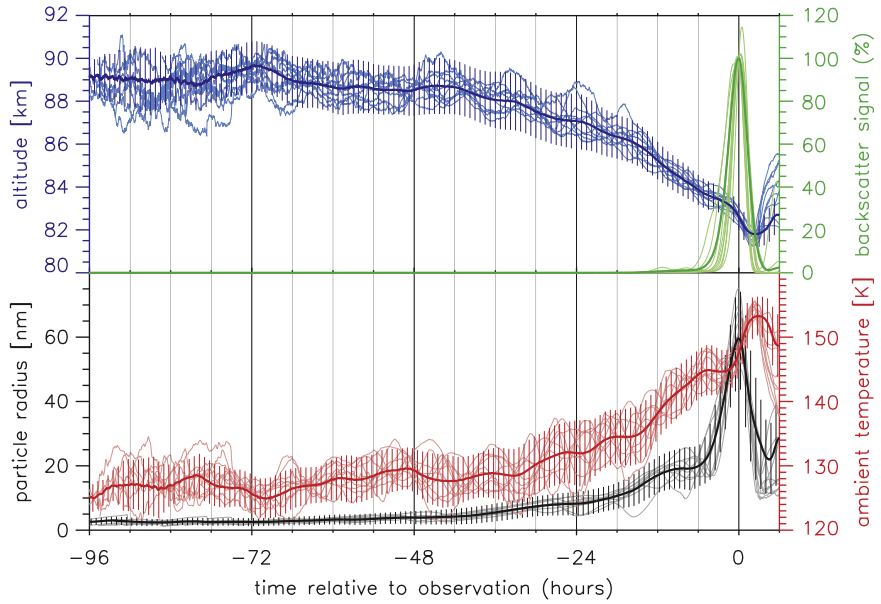

Fig. 7. Analoguous to Fig. 5, but showing those parameters as superimposed epoch analysis of 50 NLC events at ALOMAR. The thick lines show the ensemble mean, while the thin lines are individual NLC mean trajectories for the same 10 NLC also shown in Fig. 6. The vertical bars show the total variance (mean deviation of individual particle parameters from ensemble mean).

the zonal direction, as can be seen by the zonal elongation of the ellipses, e.g. at t_0-36 h. We find a mean transport distance during particle lifetime of 4500 km (zonal: $127^\circ \pm 57^\circ$, meridional: $4^\circ \pm 2^\circ$), mean lifetime will be discussed later in Section 3.2.2. We have shown above that winds from LIMA are presumably stronger by up to 15 m/s in the zonal direction and weaker by up to 6 m/s in the meridional as compared to observations (Fig. 1). Based on the local radar observations, we calculate that NLC particles have a mean transport distance of around 3000 km, including a southward transport of $\approx$1000 km. In addition, we expect the superimposed backtrajectories of several NLC to have a larger horizontal expansion than Fig. 6 suggests, since LIMA underestimates wind variability to some extent.

In Fig. 7 we show the ensemble mean and single NLC means for the microphysical and ambient parameters of Fig. 5. The single NLC events chosen represent the brightness peaks of the 10 strongest NLC, as marked in Fig. 3. The total ensemble mean has the same general shape in all parameters as the single NLC mean in Fig. 5. However, the oscillations in altitude and temperature are much less pronounced, and the peaks around t_0 in radius and backscatter signal are broader by $\approx$1 h. The lower amplitudes in altitude and temperature are caused by the superposition: While all individual NLC events are exposed to variations in background parameters much like the example in Fig. 5, these average out when calculating the ensemble mean, which is evident from the single event mean curves. The advantage of the superimposed epoch analysis is that effects occurring regularly before observing strong NLC get pronounced, i.e. the colder period about 4 h before t_0 and the sharp increase in ambient temperature around t_0.

To study in detail the physical processes leading to strong NLC, we show most of the parameters from Fig. 7 in higher temporal resolution around t_0, in Fig. 8. In the radius evolution from t_0-12 h to t_0-6 h, we find that the intermittent periods of sublimation before observation that we found when studying a single NLC event (e.g. t_0-8 h to t_0-5 h in Fig. 5) are not evident in the ensemble mean, since those occur at different times before observation for the various NLC. The broadening of the brightness and radius peak around t_0 is caused by the method of NLC event selection: Many of the strongest NLC last for 5 or 6 h. Those events near the beginning or the end of the NLC are smearing out the narrow peak. That can be seen by comparing the mean of all events to the mean of those selected at maximum brightness only (Fig. 8). This has the effect that the ensemble brightness peaks almost exactly at t_0, but the peak is broader compared to the individual NLC brightness.

To investigate the mechanism for the main particle growth phase more closely, we also show the saturation ratio S and the three components of vertical motion in Fig. 8. We note that S is considerably higher than S^* from Section 3.1.1 since S does not include the Kelvin effect, so in an $S=1$ environment particles are already sublimating. We have chosen to show S here instead of S^* since the calculation of S^* requires a microphysical model, while S can be calculated from any dynamical model that includes water vapor. During the main growth period, upward directed vertical winds cool the atmosphere and counteract the downward sedimentation of ice particles. More quantitatively, taking typical vertical winds of 8 cm/s for a period of 1 h lifts an air parcel by $\approx$300 m and leads to an adiabatic cooling of $\approx$3 K, which agrees with the observed amplitudes of temperature variations and supports the assertion that the vertical winds cause the temperature minima. The effect is that particles are extensively exposed to large amounts of water vapor. Note that at 83 km there are approximately 3 billion H_2O molecules/cm^3 whereas at 88 km there are only 50 million water molecules/cm^3. Supersaturation and particle growth peaks around 2 h prior to observation. Peak brightness occurs just after upward vertical motion terminates, which is consistent with Figure 13 in Rapp et al. (2002). After ice particles have reached their maximum size, they are exposed to strong downward directed winds which brings them out of the supersaturation region and leads to fast sublimation. Only few ice particles survive long enough to reach the next cold phase.

Turbulent transport also plays a significant role in the final growth phase, where we observe that the mean transport direction by diffusion is downward (up to -3.5 cm/s) (method I). Method II analysis shows a downward diffusion of only ≈ -1 cm/s. This difference indicates that those particles growing to larger sizes experience a stronger downward diffusion. In the earlier history (before t_0-24 h), there is a slight mean upward transport by turbulence ($\sim +2$ cm/s between t_0-24 h and t_0-72 h). The reason for this is that in order to survive for

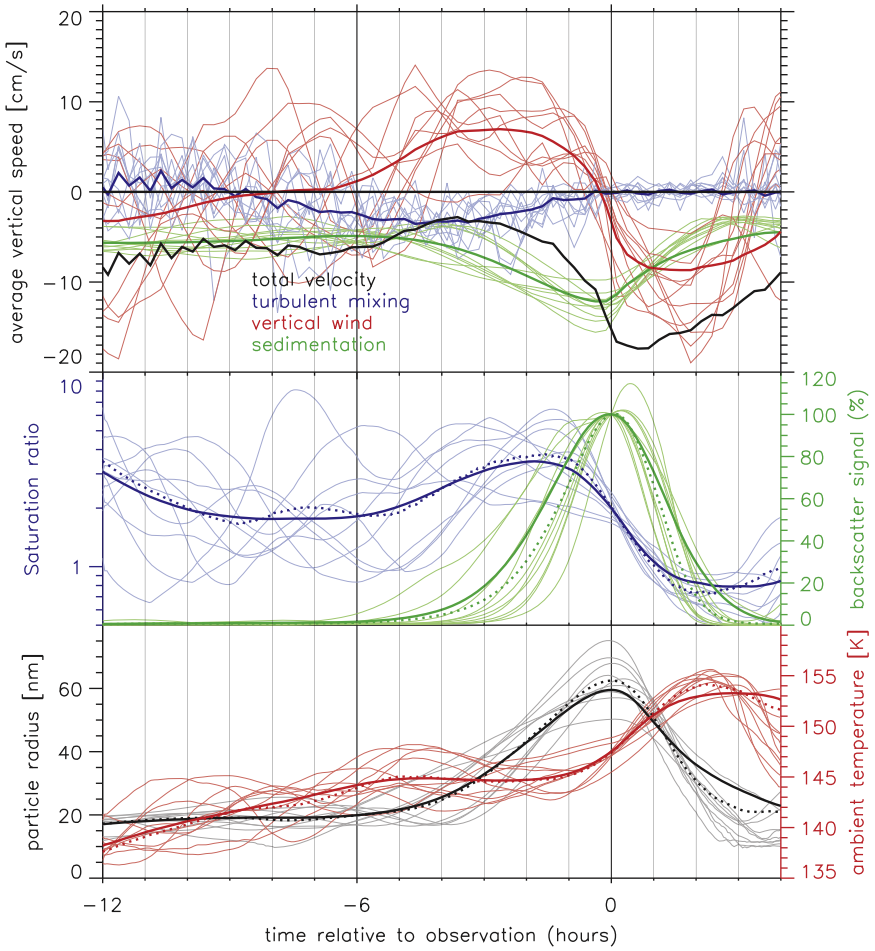

Fig. 8. Microphysical parameters during final growth phase and sublimation of NLC particles at ALOMAR. Thick lines show the 50 event ensemble mean, while the dotted lines in the middle and lower panel show the average of only those events at maximum brightness. The thin lines show the evolution of 10 NLC events selected near maximum brightness. Upper panel: Mean vertical motion (total velocity), as well as components from wind, sedimentation, and turbulent diffusion. Middle panel: Mean ambient saturation ratio (S) and backscatter signal. Lower panel: Mean particle radius and mean temperature.

a longer time, ice particles need to stay near the mesopause for an extended duration, and random upward transport helps offset sedimentation. At the same time we note that vertical wind does not play a major role in the vertical transport before the main growth phase.

The importance of turbulent downward transport and presence of a clearly defined "growth region" within the ice domain has been found recently by Megner (2011). Between t_0−4.5 h and t_0−3 h, our analysis indicates that upward directed vertical wind just compensates the speed of sedimentation and the total downward transport is due to diffusion. We also find that nucleation happens about 6–60 h before the observations, while the ice particles enter the growth region (and start becoming visible) about 5 h before observation. There is some overlap between nucleation region and growth region in the late nucleating ice particles.

We have seen that atmospheric dynamics plays a crucial role in determining growth characteristics of ice particles. We compare our results with COMMA/IAP, the precursor of LIMA, to illustrate the effect of LIMA dynamics on NLC formation (Berger and von Zahn, 2007). The main difference between these models is the adaption of ECMWF in LIMA. This greatly increases the variability of temperature and wind, which has implications for particle growth characteristics. In COMMA/IAP there are no phases of partial sublimation in between the growth phases. Therefore growth characteristics are rather different, whereas the mean particle ages are similar. By comparing our results with Figures 19 and 25 in Berger and von Zahn (2002) we find that particle growth during the last few hours before observation is significantly slower in COMMA/IAP compared to LIMA. In LIMA the visibility of NLC is mainly determined in the last few hours prior to observation, whereas it takes at least half a day in COMMA/IAP. We speculate that this is a consequence of rather smooth ambient conditions combined with a stronger mean upward wind in COMMA/IAP. Another consequence of this difference in dynamics is that most LIMA ice particles nucleate around the mesopause while they nucleate between 84 and 86 km in COMMA/IAP.

3.2. *Nucleation process, sublimation and visibility time for NLC at 69°N*

We now investigate the age of mesospheric ice particles, the conditions required for particle nucleation, and the sublimation process at the end of their life cycle. The physical processes become more clear when concentrating on one event first.

3.2.1. *Nucleation process of a single NLC observed at ALOMAR (69°N)*

In Fig. 9 we show the nucleation rate for the ice particles of the single NLC on July 14, 7 UT. In contrast to the previous section,

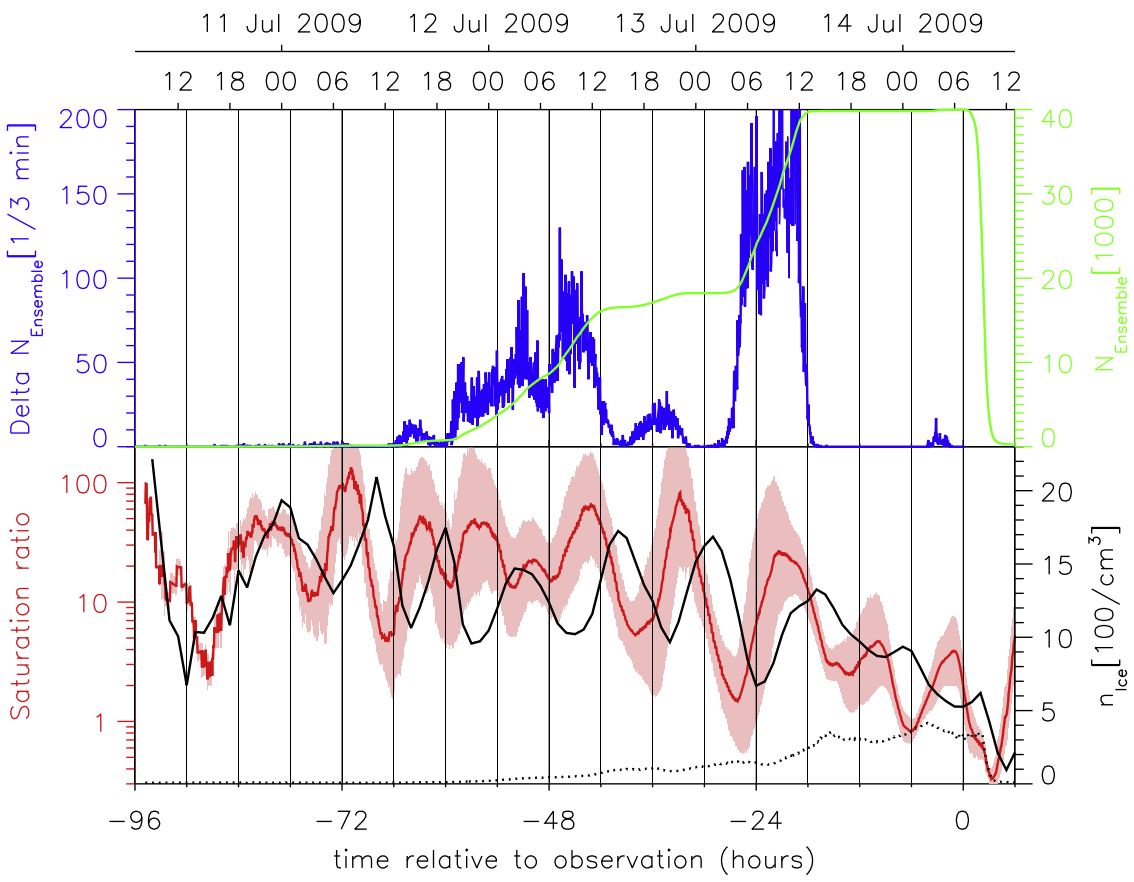

Fig. 9. Particle nucleation and growth for the NLC of July 14, 7 UT. Upper panel: The nucleation rate (blue) is the differential of the green curve (the number of particles present). Lower panel: Mean and distribution width of ambient saturation ratio, calculated over log S (red), mean number density of ice particles including the particles of the ensemble (solid black, right scale), and mean number density of ensemble ice particles (dotted black, right scale). (For interpretation of the references to color in this figure caption, the reader is referred to the web version of this article.)

this is done with method II (without weighting with $\beta(t_0)$), since we focus on the mechanisms first before deriving quantitative values in Section 3.2.2. In the upper panel, we see that nucleation of the ice particles forming the NLC occurs not continuously, but in bursts with typical durations of $\approx$6 h. These bursts are separated by time periods with little or no new particles forming. To find the cause for these nucleation bursts, we look into the ambient conditions surrounding these ice particles. The lower panel shows the ambient saturation ratio (without the Kelvin effect). We define the ambient of an ice particle as the model grid volume (about 100 km $\times$ 100 km horizontally and 100 m vertically) surrounding the particle.

Also shown in Fig. 9 are ice particle number density n_{ice} and ensemble number density $n_{ice,\mathrm{Ensemble}}$. n_{ice} is calculated from the total number of model ice particles in the particle's ambient. Similarly, $n_{\mathrm{ice,Ensemble}}$ is calculated from the number of ensemble members in the ambient. n_{ice} also includes those particles that have evaporated until t_0. At t_0 the ratio $n_{\mathrm{ice,Ensemble}}/n_{\mathrm{ice}}$ reflects the ratio of ice particles used in the analysis to all ice particles in the volume. Before t_0, this ratio shows for example that only 1 % of the ice particles found in the NLC at t_0-60 h are later analyzed at t_0.

We note that ice nucleation takes place when supersaturation is increasing, since available condensation nuclei will create icy particles as soon as ambient supersaturation reaches their individual Kelvin barrier, dependent on the nuclei's size. However, we found one example where nucleation occurs in spite of decreasing mean S around t_0-48 h. This is caused by a combination of factors: Inhomogeneities of saturation ratio within the ice cloud, turbulent motion of single particles into higher saturated areas and dust particle relocation. The spread of S within the cloud is significant, as can be seen in the lower panel of Fig. 9.

We now investigate the age in general, i.e. why are there virtually no particles older than 4 days? To understand the vastly different nucleation rates between the bursts, we have to consider what affects nucleation rate other than the saturation ratio. n_{ice} is mostly following the oscillation in S with a delay of about 3 h. It means that there is a continuous process of nucleating and sublimating going on, with sublimating particles making their nuclei available for subsequent nucleation. An old ice particle must have survived many low S periods, which gets more and more unlikely the older the particles are. From our simulations we find that the oldest of 40,000 particles gets 95 h old.

In Fig. 9 we see that the magnitude of the bursts varies by two orders of magnitude from about $\Delta N/\Delta t = 2/3$ min around t_0-72 h to about $\Delta N/\Delta t = 150/3$ min at t_0-24 h. The reason for the different scales of the nucleation bursts partly lies in the low S periods preceding it: At t_0-26 h, supersaturation is particularly low, causing many ambient ice particles to sublimate. As a result, there are a lot of potential nuclei available to start the strong nucleation burst around t_0-24 h. We observe that a saturation ratio of $S\approx 10$ already leads to significant sublimation. For example, the local maxima of n_{ice} in Fig. 9 are found at $S\approx 20$. On the other hand the start of the nucleation bursts is found at saturation values of $S=3$–10. This result is counterintuitive on the first glance. However when taking the Kelvin effect into account (Fig. 5) we already observed that the ambient S is only a rough indicator for growth and sublimation of ice particles.

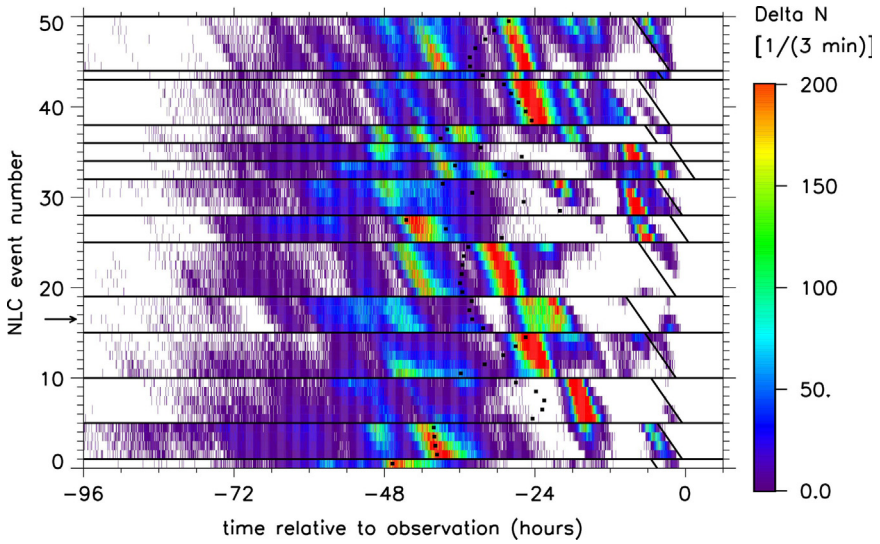

Fig. 10. Rate of nucleation for all 50 events at ALOMAR (similar to the blue curve of Fig. 9). The NLC events are in chronological order, from July 5, 5 UT as no. 1 to July 31, 8 UT as no. 50. The 14 different NLC (Fig. 3) are separated by horizontal bars. The black dots show mean NLC particle age (not weighted). The slanted lines around $t=0$ show midnight in universal time. The July 14, 7 UT NLC is no. 17 (arrow).

3.2.2. Nucleation of 50 NLC events at 69°N

Bearing in mind the rather complex interplay of the different ambient conditions leading to bursts of nucleation we now investigate all 50 events to estimate the mean particle age and the robustness of the occurrence of nucleation bursts. We show the nucleation rate for all 50 ALOMAR NLC events in Fig. 10, again without signal-weighting. We see that burst nucleation is prevalent for all cases within the ensemble. For the 14 different NLC we find multiple nucleation bursts, where the strongest bursts occur 12–36 h before t_0. The nucleation bursts of multiple events from the same NLC are mostly shifted by the time interval between their observation, resulting in a slanted appearance of the bursts. As for the single event case, the bursts are less pronounced during early nucleation. To quantify the mean age of particles in the NLC we calculate the mean of the time period from nucleation to t_0 of the 40,000 particles analyzed. We find that the mean particle age ranges from about 48 h to 18 h. The age spread of the events in each NLC is up to 24 h, indicating that the particle age gives only a qualitative measure of the clouds' formation.

In Fig. 11 we combine the nucleation time of all particles in 50 NLC events with the altitude of nucleation. Using method I, we calculate mean particle age as 36 h with a distribution width of 16 h. However as discussed above, the mean and especially the width are only a qualitative measure due to the skewness of the age distribution. The mean nucleation altitude is 87.7 km with a distribution width of 1.6 km. Particle age and nucleation altitude are correlated (correlation coefficient $CC=0.75$): Generally, older particles nucleate higher, near the mesopause (see also Fig. 7), while younger particles are formed at lower altitudes. We also show particle age and the nucleation altitude without signal-weighting in Fig. 11 (method II). This shows primarily the origin of the large number of smaller particles which contribute only slightly to the NLC visibility. The mean age calculated by this analysis method is ≈ 32 h, which is also the value we would achieve by averaging over the single NLC age shown in Fig. 10. Late nucleating particles have less time to grow, so if they nucleate outside the region of very favorable growth conditions, they will not grow big and hence do not contribute to the NLC visibility.

The results of the two different analysis methods (I) signal weighted, favoring large particles and (II) without signal weighting, favoring small particles can be easily compared by looking at the ellipses in Fig. 11. The center of the ellipses indicates the mean of the distribution, while the semiaxes indicate the variance. Additionally the orientation of the semi-major axis indicates the covariance of age and altitude. By comparing the ellipses of method I and II we find that larger particles are about 4 h older than the smaller particles but nucleate at roughly the same altitude. The covariances of age and altitude for larger (I) and smaller (II) particles are nearly identical. Despite this small difference of the mean age and nucleation altitudes of small and large particles we observe that the nucleation altitudes of late nucleating particles (after t_0-24 h) differ significantly. We find that late nucleating particles only grow to large sizes if they nucleate in a limited altitude range with a high anticorrelation of time relative to observation and altitude.

Since the distribution of condensation nuclei in the model does not include dust particles smaller than $r_{cutoff}=1.2$ nm, there might be a bias in the results. We generally do not find any significant relation between parameters concerning ice nucleation and those concerning NLC around t_0 as discussed in the next section ($|CC|<0.1$), so we expect the final growth phase to be unaffected by this bias. To estimate the effect on the mean particle age we analyzed the dependence of the age on the radius of the dust particles in the present simulations. Using this approach we find that our mean age might be underestimated by up to 10% when lowering r_{cutoff} to 0.7 nm, comparable to the difference between methods I and II.

3.2.3. Sublimation, visibility time and other parameters at 69°N

Not shown, but calculated in the same way are time and altitude of sublimation, that is the particles' lifetime after t_0 and the altitude where they disappear. Visible (and thus, large) particles sublimate quickly after reaching their maximum size (see also Fig. 7). Time to sublimation is 2.3 ± 1.1 h (method I), while the unweighted lifetime after t_0 is 3.8 ± 3.1 h. The reason for this is the difference in altitude at t_0: Small particles are located higher up within the NLC and can thus survive longer, so many of them are still around 6 h after observation. Small particles also sediment more slowly than large ones, but the effect of this on sublimation time is compensated by their smaller

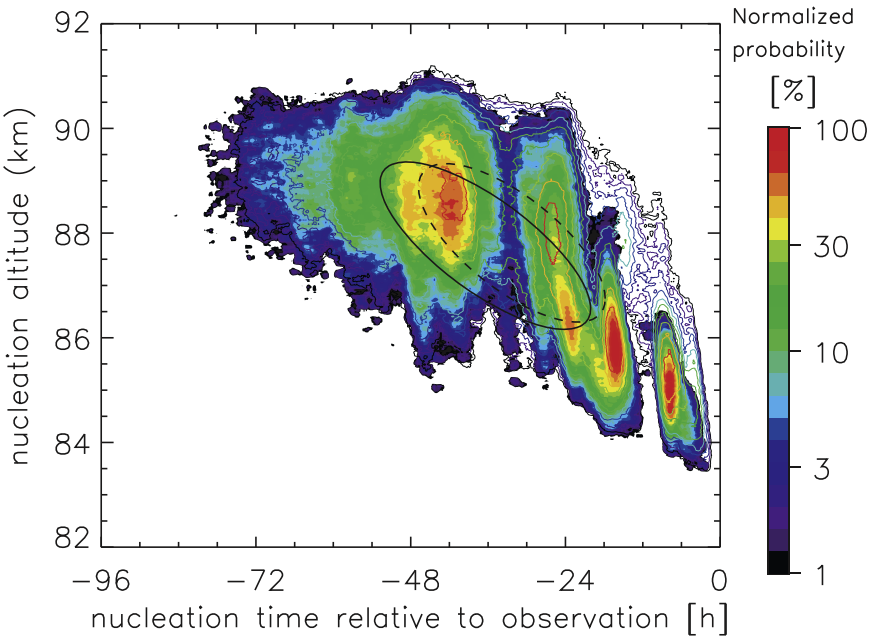

Fig. 11. Two-dimensional histogram of the nucleation time and altitude of particles observed around 69°N. The filled contours show the distribution weighted by the backscatter signal, favoring large particles (method I). The contour lines show the actual distribution, favoring small particles (method II). Both distributions are normalized to maximum value. Solid ellipses indicate mean and width of the weighted distribution, dashed those of the unweighted distribution. The ellipse orientation is calculated from the covariance and indicates an anticorrelation of nucleation altitude and nucleation time.

size. For the typical altitude of the sublimation process, we find 81.3 ± 0.36 km. This agrees well with the measured lower edge of NLC. Kaifler et al. (2011) found a mean lower edge of 82.1 km, however they included weak and strong NLC. In 2009, the ALOMAR RMR-lidar measured a mean lower edge of strong NLC of 80.9 ± 0.9 km. The good agreement supports our analysis method and our understanding of the processes in the cloud.

To characterize the rapid particle growth before the observation, we determined the time when ice particles in their growth phase exceed 10% of their backscatter signal at t_0. We arrive at 2.8 ± 1.4 h, which means that most particles reach visible size $\approx 1-5$ h before being observed. We define the particle visibility time as the time that a particle is above the 10% of $\beta(t_0)$ threshold from growth to sublimation. In Fig. 12, we show this time period together with the particle size at observation. For larger particles (Method I) the mean particle visibility time is 4.4 ± 1.7 h, during which the particles are transported a mean distance of about 22° westward and 1° southward, corresponding to a distance of ≈ 850 km. Considering smaller particles (Method II) we get 7.7 h. We have performed a similar analysis selecting very large particles ($r > 80$ nm) and find a visibility period of only ≈ 3 h. So larger particles have a shorter visibility time than smaller ones. This can also be seen by the ellipses in Fig. 12. The different orientations of the ellipses of larger and smaller particles indicates that the relation is not linear to the particle size, most likely because the visibility time depends on the backscatter signal ($\beta \propto r^5$). Similarly, we have used a radius threshold of $r = 20$ nm. We find that the mean time above $r = 20$ nm is 8 h. Particles that reach about $r = 55$ nm at t_0 are larger than $r = 20$ nm for the longest time period. While it is trivial that smaller particles spend a shorter time above $r = 20$ nm, we think that particles that reach sizes above $r = 55$ nm at t_0 need rapid cooling, which is probably followed by rapid warming. We conclude that most NLC particles are visible for $\approx 3-6$ h, but spend about 8 h above the $r = 20$ nm threshold.

The results of method I (large particles) and method II (small particles) indicate that method I using signal weighted distributions gives representative mean values for large particles, contributing most to the "visible" NLC. As we are interested in the conditions that lead to the formation of clouds actually observable by instruments, we mainly give values analyzed using method I, which was used in all Section 3 figures except Figs. 9 and 10. There are a number of ambient parameters responsible for forming noctilucent clouds. In Table 1 we give some parameters in addition to those discussed before, like particle size and altitude at observation and 24 h before. We also give an estimate for the statistical uncertainty of these values, derived from the spread of independent single NLC mean values. For example we find that clouds observed at ALOMAR typically form at a temperature of (130 ± 5)K and sublimate at (156 ± 2) K, while ambient temperature around observation is 148 ± 3 K.

3.3. Results from other latitudes

We extend our analysis to the other two latitude regimes, namely Spitsbergen and low latitudes (south of 60°N). We show nucleation and growth characteristics for these latitudes and discuss the similarities as well as the differences compared to the ALOMAR case.

3.3.1. Spitsbergen (78°N)

In Fig. 13 we show ambient and microphysical parameters as well as the nucleation time and altitude for ice particles observed at Spitsbergen. The first thing we note is that the general shapes of the time series for radius, altitude/temperature and backscatter signal are similar compared with 69°N. However, we find that at the beginning of their life cycle, the period where ice particles are quasi-stationary near the mesopause is much longer. To validate our modeling in this altitude range we compared the mean nucleation temperature (Table 1) of about 124 K around 89.5 km altitude with results from Höffner and Lübken (2007). They found a mean temperature of 122.5 ± 1 K (DOY 180–210) which agrees nicely to the model results.

The mean age of particles at 78°N is 63 ± 15 h, more than a day older compared to particles at 69°N. There are two reasons for

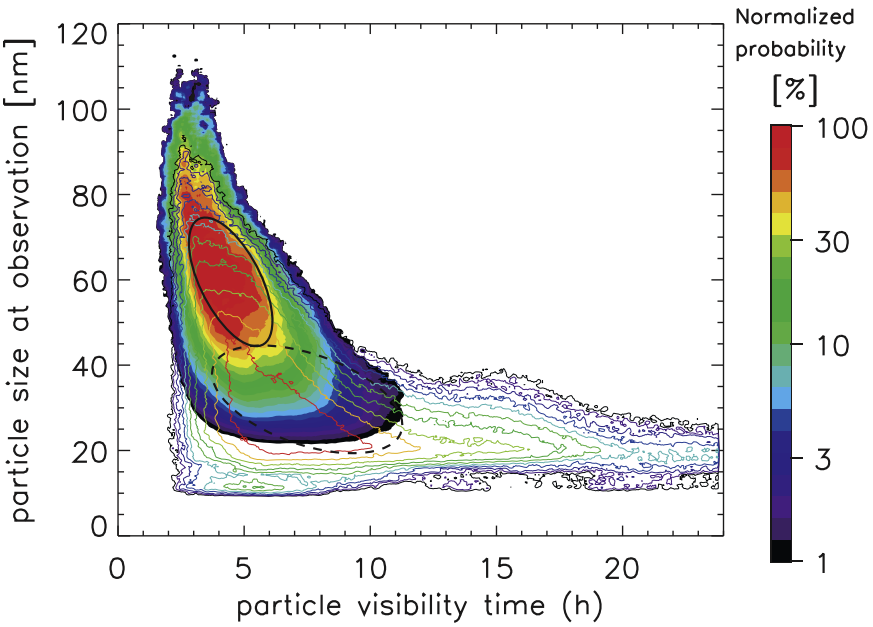

Fig. 12. Two-dimensional histogram of visibility time vs particle size at t_0. Filled contours show the signal weighted distribution (method I), while contour lines show the actual distribution (method II). Ellipses indicate mean, distribution width and covariance of the weighted (solid line) and actual (dashed line) distributions.

Table 1
Mean values and distribution width for selected parameters of ice particle evolution. Unmarked values are signal-weighted (method I). Values in parentheses are estimates for the statistical uncertainty of the mean. The top seven parameters are synchronous in time, those below are taken at individual times for each particle.

Observation latitude	$<60^\circ$N	69°N	78°N
Observation radius	37.4 ± 8.6 (1.6) nm	59.5 ± 15.1 (2.2) nm	61.3 ± 16.1 (2.7) nm
Observation radius[a]	24.0 ± 8.4 nm	31.9 ± 12.6 nm	39.3 ± 11.9 nm
Observation altitude	83.1 ± 0.8 (0.11) km	82.6 ± 0.6 (0.08) km	82.9 ± 0.6 (0.09) km
Observation temperature	143.9 ± 3.8 (0.4) K	147.5 ± 3.3 (0.3) K	148.6 ± 3.6 (0.4) K
Radius at t_0-24 h	6.0 ± 3.5 (0.7) nm	8.2 ± 3.7 (0.7) nm	10.6 ± 3.3 (0.4) nm
Altitude at t_0-24 h	87.5 ± 1.0 (0.3) km	87.1 ± 1.3 (0.3) km	86.5 ± 1.3 (0.14) km
Temperature at t_0-24 h	132.0 ± 3.4 (0.9) K	132.0 ± 5.1 (1.3) K	132.5 ± 5.4 (0.9) K
Age at observation	19.3 ± 8.3 (2.2) h	36.4 ± 16.4 (2.4) h	63.0 ± 15.0 (1.6) h
Nucleation altitude	87.0 ± 1.1 (0.2) km	87.8 ± 1.6 (0.3) km	89.4 ± 1.2 (0.07) km
Nucleation temperature	132.5 ± 3.0 (0.5) K	130.0 ± 4.4 (0.5) K	124.1 ± 3.6 (0.3) K
Sublimation time	1.8 ± 0.9 (0.12) h	2.3 ± 1.1 (0.2) h	2.8 ± 1.3 (0.18) h
Sublimation altitude	81.6 ± 0.5 (0.11) km	81.3 ± 0.4 (0.07) km	81.6 ± 0.3 (0.07) km
Sublimationtemperature	154.3 ± 1.9 (0.4) K	156.3 ± 1.4 (0.15) K	157.1 ± 1.4 (0.13) K
Visibility time	4.8 ± 1.5 (0.3) h	4.5 ± 1.7 (0.4) h	4.6 ± 2.0 (0.3) h

[a] Values are derived by method II, preferring small particles.

this: The ambient saturation ratio S around the mesopause is somewhat higher closer to the pole (not shown). Additionally the single event ambient temperature variations (thin lines in Fig. 13) are smaller compared to the ALOMAR case. Together, this has the effect that periods of very low S are rare, so permanent supersaturation is achieved even during the warm phase of waves, leading to the observed continuous particle nucleation at high altitude.

Because of the higher particle age, we observe a mean lifetime transport of $237^\circ \pm 60^\circ$ westward and $2.3 \pm 1.5^\circ$ southward. This corresponds to a distance of 5100 km. The particles nucleate at a mean altitude of 89.4 km, which is 1.6 km higher than at 69°N. Comparing Figs. 11 and 13 we conclude that the main reason for this is that nucleation of almost all particles growing to visible sizes occurs very early, around the mesopause. Burst nucleation is less pronounced here and is in fact only observed for those few particles that nucleate below ≈ 88 km. This lack of nucleation bursts is another consequence of the smaller variability in the background conditions encountered by ice particles at these latitudes.

The visibility time at 78°N as described in Section 3.2.3 is 4.6 ± 2 h, which is comparable to the results at ALOMAR. This means that the lifetime difference of ≈ 27 h has no bearing on the final growth phase from 20–60 nm, which occurs in the same timeframe as at ALOMAR.

In general, the evolution of ice particle parameters (altitude, ambient temperature, radius and backscatter signal) is very similar between 69°N and 78°N. The two cases differ markedly only during the time before particles reach visible size. During the main growth phase a few hours before observation, there is little difference between NLC at the two locations. This means that the visible part of noctilucent cloud formation is basically the same at Spitzbergen as at ALOMAR.

3.3.2. *Latitudes below 60°N*

In Fig. 14 we show the evolution of ambient and microphysical parameters at latitudes south of 60°N (see also Table 1). There are

a number of differences compared to higher latitudes: The mean radius at the time of observation is much smaller than at 69°N and 78°N. We note that our selection (Section 2.1) includes

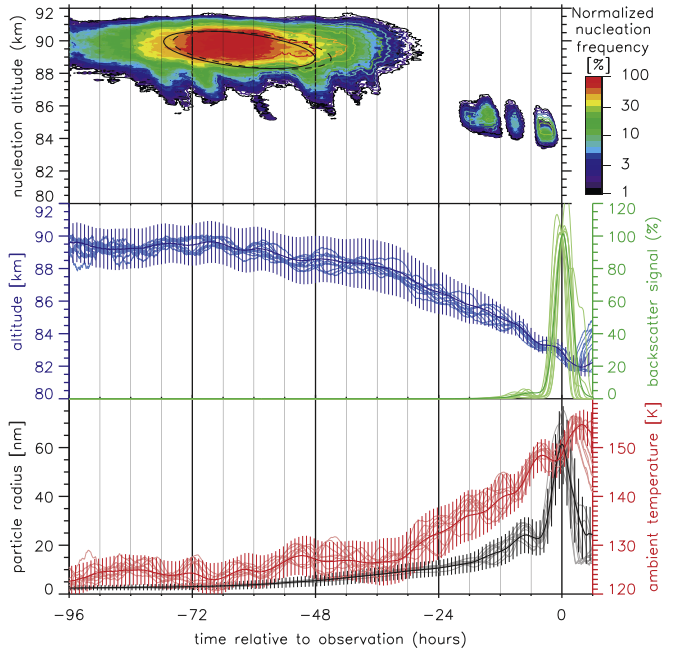

Fig. 13. Results of a 50 event superimposed epoch analysis of NLC observed at 78°N, 11°E. Upper panel: Nucleation time and altitude. Middle and lower panel: Temporal evolution of ambient and particle properties. For further explanations see captions of Figs. 7 and 11.

weaker NLC for low latitudes, hampering the comparison of different latitudes. The overall shape of the time series is again similar to those at higher latitudes, but the lower latitude NLC experience radically changing ambient conditions, as can be seen from the spread of the thin lines in Fig. 14 compared to Fig. 7. At the same time the saturation ratio is lower than at ALOMAR. This has the effect that the period of stationarity at the beginning of ice particle life cycle is almost completely absent. Because of the high variations in temperature, ice particles need to grow quickly, as their chance to survive warm periods is lower. Most particles that nucleate do not grow large enough to become visible. This results in a much smaller particle age of 19 ± 8 h seen in Fig. 14. The visibility time on the other hand is 4.8 ± 1.5 h, slightly higher than at the other latitudes. The altitude of particle nucleation is 87 ± 1 km, about 1 km lower than at 69°N.

When comparing the time and altitude of nucleation (Figs. 14 vs. 11), we again see nucleation in bursts. The fact that we observe this feature south of 60°N and for ALOMAR ice clouds, but not for NLC at Spitsbergen, is an indication that waves play a significant role in determining the age of the particles. However their effect is suppressed at altitudes of permanent high supersaturation.

Generally, NLC at latitudes below 60°N are highly affected by background variations. This sensitive dependence on ambient conditions results in much lower lifetimes. It also means that the ice particles nucleate closer to the point of observation compared to those forming NLC at 69°N. This has no bearing on visible NLC characteristics, which are comparable to the ALOMAR case. We also found that the NLC are accompanied with southward directed transport of 150–500 km in the last 6 h before t_0. Similarly, Gerding et al. (2007) found that strong southward

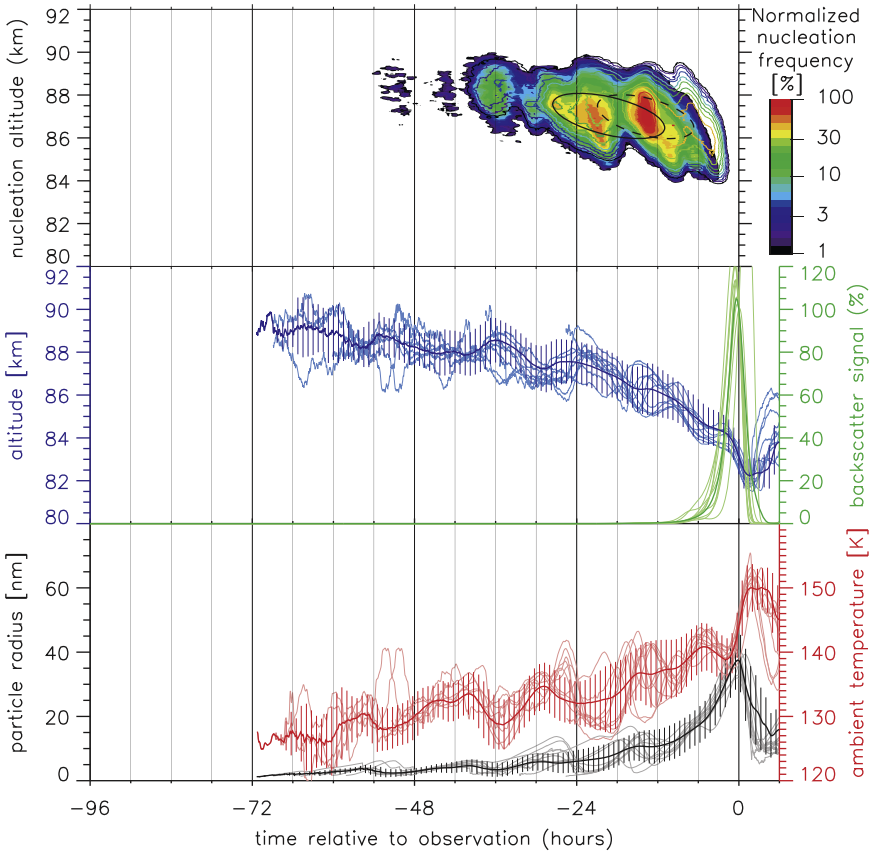

Fig. 14. Superimposed epoch analysis for NLC observed at several locations south of the 60°N latitude circle. Upper panel: Particle age and nucleation altitude distribution. Middle and lower panel: Evolution of particle properties and temperature. The beginning of the time series (at t_0-71 h) is the age of the oldest particle. For more details see captions of Figs. 7 and 11.

winds are a precondition for NLC at Kühlungsborn (54°N). They estimated a southward transport of 400 km in the last 6 h.

4. Summary and conclusions

We analyze particle nucleation and evolution of NLC arriving around ALOMAR (69°N, 16°E) and two other locations at higher and lower latitudes. We characterize the ambient conditions of ice nucleation and growth, as well as the typical life cycle of NLC particles including time scales for a selection of strong NLC events, weighting the individual trajectories with their backscatter signal to emphasize visible ice particles.

Concerning the typical evolution of ice particles, we observe that particle nucleation starts slightly below the mesopause ($\approx$88 km) and occurs in bursts (less pronounced at 78°N) within areas of high supersaturation. These bursts are caused by flow through the variable background of temperature and H_2O. Nucleation is followed by a generally slow but steady growth during the first part of their life cycle. By a combination of sedimentation, diffusion, and vertical winds, particles eventually reach the growth zone around 84 km. Those particles reaching this altitude during cold phases of the wave activity are exposed to both supersaturation and upward winds to delay their sedimentation. This allows quick ice particle growth because of the high water vapor concentration at this altitude. Around the time of maximum NLC brightness or up to 1 h before (<60°N), vertical wind turns to downward and accelerates sedimentation to warmer altitudes and particle sublimation.

Typical particle lifetimes at 69°N are $\approx$36 h. Particles observed at 78°N are older and those below 60°N are younger. The time period of visibility is only $\approx$5 h however, basically independent of observational latitude. This implies that the main characteristics of NLC observed by lidar are formed in the last few hours before observation. Since this occurs close to the observation point, study of background conditions at the observation site are important and representative for understanding the final NLC growth phase.

We intend to further investigate how far these results also apply to weaker NLC, by choosing a different time frame rather than just mid season in a strong NLC year. Also, we will look into the cause of those nucleation bursts and investigate the role of dynamics and microphysics in the cloud evolution.

Acknowledgments

We thank the DFG for their financial support of the CAWSES priority program. The European Centre for Medium-Range Weather Forecasts (ECMWF) is gratefully acknowledged for providing ERA-40 and operational analysis data.

References

Bardeen, C.G., Toon, O.B., Jensen, E.J., Hervig, M.E., Randall, C.E., Benze, S., Marsh, D.R., Merkel, A., 2010. Numerical simulations of the three-dimensional distribution of polar mesospheric clouds and comparisons with Cloud Imaging and Particle Size (CIPS) experiment and the Solar Occultation For Ice Experiment (SOFIE) observations. Journal of Geophysical Research 115, 10204.

Baumgarten, G., Fiedler, J., Rapp, M., 2010. On microphysical processes of noctilucent clouds (NLC): observations and modeling of mean and width of the particle size-distribution. Atmospheric Chemistry and Physics 10, 6661–6668.

Baumgarten, G., Fiedler, J., von Cossart, G., 2007. The size of noctilucent cloud particles above ALOMAR (69N,16E): optical modeling and method description. Advances in Space Research 40, 772–784.

Baumgarten, G., Thomas, G.E., 2006. The importance of ice particle shape on UV measurements of polar mesospheric clouds: SBUV/2 observations. Journal of Atmospheric and Solar-terrestrial Physics 68, 78–84.

Berger, U., 2008. Modeling of middle atmosphere dynamics with LIMA. Journal of Atmospheric and Solar-terrestrial Physics 70, 1170–1200.

Berger, U., von Zahn, U., 2002. Icy particles in the summer mesopause region: three-dimensional modeling of their environment and two-dimensional modeling of their transport. Journal of Geophysical Research 107, 1366.

Berger, U., von Zahn, U., 2007. Three-dimensional modeling of the trajectories of visible noctilucent cloud particles: an indication of particle nucleation well below the mesopause. Journal of Geophysical Research 112, 16204.

Chandran, A., Rusch, D.W., Thomas, G.E., Palo, S.E., Baumgarten, G., Jensen, E.J., Merkel, A.W., 2012. Atmospheric gravity wave effects on polar mesospheric clouds: a comparison of numerical simulations from CARMA 2D with AIM observations. Journal of Geophysical Research (Atmospheres) 117, 20104.

Espy, P.J., Jutt, H., 2002. Equilibrium temperature of water-ice aerosols in the high-latitude summer mesosphere. Journal of Atmospheric and Solar-terrestrial Physics 64, 1823–1832.

Fiedler, J., Baumgarten, G., Berger, U., Hoffmann, P., Kaifler, N., Lübken, F.-J., 2011. NLC and the background atmosphere above ALOMAR. Atmospheric Chemistry and Physics 11, 5701–5717.

Fiedler, J., Baumgarten, G., Lübken, F.-J., 2009. NLC observations during one solar cycle above ALOMAR. Journal of Atmospheric and Solar-terrestrial Physics 71, 424–433.

Gerding, M., Höffner, J., Rauthe, M., Singer, W., Zecha, M., Lübken, F.-J., 2007. Simultaneous observation of noctilucent clouds, mesospheric summer echoes, and temperature at a midlatitude station (54°N). Journal of Geophysical Research 112, D12111.

Gumbel, J., Witt, G., 2001. Rocket-borne photometry of NLC particle populations. Advances in Space Research 28, 1053–1058.

Hervig, M.E., Gordley, L.L., 2010. Temperature, shape, and phase of mesospheric ice from Solar Occultation for Ice Experiment observations. Journal of Geophysical Research 115, 15208.

Hervig, M.E., Gordley, L.L., Stevens, M.H., Russell III, J.M., Bailey, S.M., Baumgarten, G., 2009. Interpretation of SOFIE PMC measurements: cloud identification and derivation of mass density, particle shape, and particle size. Journal of Atmospheric and Solar-terrestrial Physics 71, 316–330.

Hoffmann, P., Becker, E., Singer, W., Placke, M., 2010. Seasonal variation of mesospheric waves at northern middle and high latitudes. Journal of Atmospheric and Solar-terrestrial Physics 72, 1068–1079.

Höffner, J., Lübken, F.-J., 2007. Potassium lidar temperatures and densities in the mesopause region at Spitsbergen (78°N). Journal of Geophysical Research 112, 20114.

Hunten, D.M., Turco, R.P., Toon, O.B., 1980. Smoke and dust particles of meteoric origin in the mesosphere and stratosphere. Journal of the Atmospheric Sciences 37, 1342–1357.

Jesse, O., 1889. The luminous night-clouds. The Astronomical Journal 8, 191–192.

Kaifler, N., Baumgarten, G., Fiedler, J., Latteck, R., Lübken, F.-J., Rapp, M., 2011. Coincident measurements of PMSE and NLC above ALOMAR (69° N, 16° E) by radar and lidar from 1999-2008. Atmospheric Chemistry and Physics 11, 1355–1366.

Li, Q., Rapp, M., Röttger, J., Latteck, R., Zecha, M., Strelnikova, I., Baumgarten, G., Hervig, M., Hall, C., Tsutsumi, M., 2010. Microphysical parameters of mesospheric ice clouds derived from calibrated observations of polar mesosphere summer echoes at Bragg wavelengths of 2.8 m and 30 cm. Journal of Geophysical Research 115, D00I13.

Lübken, F., Berger, U., Baumgarten, G., 2009. Stratospheric and solar cycle effects on long-term variability of mesospheric ice clouds. Journal of Geophysical Research 114, D00I06.

Lübken, F.-J., Baumgarten, G., Fiedler, J., Gerding, M., Höffner, J., Berger, U., 2008. Seasonal and latitudinal variation of noctilucent cloud altitudes. Geophysical Research Letters 35, 6801.

Lübken, F.-J., Berger, U., 2011. Latitudinal and interhemispheric variation of stratospheric effects on mesospheric ice layer trends. Journal of Geophysical Research 116, D00P03.

Lübken, F.-J., Berger, U., Kiliani, J., Baumgarten, G., Fiedler, J., 2013. Solar variability and trend effects in mesospheric ice layers. In: Lübken, F.-J. (Ed.), Climate and Weather of the Sun-Earth System (CAWSES). Springer, Dordrecht, pp. 317–338.

McClintock, W.E., Rusch, D.W., Thomas, G.E., Merkel, A.W., Lankton, M.R., Drake, V.A., Bailey, S.M., Russell III, J.M., 2009. The cloud imaging and particle size experiment on the Aeronomy of Ice in the mesosphere mission: instrument concept, design, calibration, and on-orbit performance. Journal of Atmospheric and Solar-Terrestrial Physics 71, 340–355.

Megner, L., 2011. Minimal impact of condensation nuclei characteristics on observable Mesospheric ice properties. Journal of Atmospheric and Solar-Terrestrial Physics 73, 2184–2191.

Merkel, A.W., Marsh, D.R., Gettelman, A., Jensen, E.J., 2009. On the relationship of polar mesospheric cloud ice water content, particle radius and mesospheric temperature and its use in multi-dimensional models. Atmospheric Chemistry and Physics 9, 8889–8901.

Nussbaumer, V., Fricke, K.H., Langer, M., Singer, W., von Zahn, U., 1996. First simultaneous and common volume observations of noctilucent clouds and polar mesosphere summer echoes by lidar and radar. Journal of Geophysical Research 101, 19161–19168.

Pruppacher, H.R., Klett, J.D., Sartor, D., 1978. Microphysics of Clouds and Precipitation.

Rapp, M., Lübken, F.-J., 2004. Polar mesosphere summer echoes (PMSE): review of observations and current understanding. Atmospheric Chemistry and Physics 4, 2601–2633.

Rapp, M., Lübken, F.-J., Müllemann, A., Thomas, G.E., Jensen, E.J., 2002. Small-scale temperature variations in the vicinity of NLC: experimental and model results. Journal of Geophysical Research 107, 4392.

Rapp, M., Thomas, G.E., Baumgarten, G., 2007. Spectral properties of mesospheric ice clouds: evidence for non-spherical particles. Geophysical Research Letters 112, D03211.

Russell III, J.M., Bailey, S.M., Gordley, L.L., Rusch, D.W., Horányi, M., Hervig, M.E., Thomas, G.E., Randall, C.E., Siskind, D.E., Stevens, M.H., Summers, M.E., Taylor, M.J., Englert, C.R., Espy, P.J., McClintock, W.E., Merkel, A.W., 2009. The Aeronomy of Ice in the Mesosphere (AIM) mission: overview and early science results. Journal of Atmospheric and Solar-Terrestrial Physics 71, 289–299.

Stevens, M.H., Englert, C.R., DeLand, M.T., Bailey, S.M., 2007. Polar mesospheric cloud mass and the ice budget: 2. Application to satellite data sets. Journal of Geophysical Research 112, 8205.

Stevens, M.H., Siskind, D.E., Eckermann, S.D., Coy, L., McCormack, J.P., Englert, C.R., Hoppel, K.W., Nielsen, K., Kochenash, A.J., Hervig, M.E., Randall, C.E., Lumpe, J., Bailey, S.M., Rapp, M., Hoffmann, P., 2010. Tidally induced variations of polar mesospheric cloud altitudes and ice water content using a data assimilation system. Journal of Geophysical Research 115, 18209.

Thomas, G.E., McKay, C.P., 1985. On the mean particle size and water content of polar mesospheric clouds. Planetary and Space Science 33, 1209–1224.

Turco, R.P., Toon, O.B., Whitten, R.C., Keesee, R.G., Hollenbach, D., 1982. Noctilucent clouds – simulation studies of their genesis, properties and global influences. Planetary and Space Science 30, 1147–1181.

von Zahn, U., Berger, U., 2003. Persistent ice cloud in the midsummer upper mesosphere at high latitudes: three-dimensional modeling and cloud interactions with ambient water vapor. Journal of Geophysical Research 108, 8451.